Available online at www.sciencedirect.com

ScienceDirect

Advances in Space Research 76 (2025) 5406–5418

ADVANCES IN SPACE RESEARCH (a COSPAR publication)

www.elsevier.com/locate/asr

Radiation-induced degradation in the properties of pristine and double-walled carbon nanotube-enhanced poly(2,5-benzimidazole) polymers for radiation shielding in the LEO

Bosco Oryema [a,b,*], Lynndle Square [a], Ernst Ellis [a]

[a] Centre for Space Research, North-West University, Potchefstroom 2531 North West, South Africa
[b] Department of Physics, Muni University, Arua, P.O. Box 725, West Nile, Uganda

Received 17 May 2025; received in revised form 14 July 2025; accepted 26 August 2025
Available online 1 September 2025

Abstract

Degradation in the properties of polymer-based materials in space environments is a critical challenge for developing lightweight radiation shielding solutions. In this paper, a comparative study of the impacts of helium ion (He^+) irradiation one of the ion species in the Low Earth Orbit (LEO) environment on the structural and optical properties of pristine and 1.0 wt% double-walled carbon nanotube (DWCNT)-enhanced poly(2,5-benzimidazole) (ABPBI) polymers for LEO radiation shielding applications was conducted. The two polymer categories were separately chemically prepared in the laboratory, moulded, dried, and cut into 1 cm × 1 cm pieces, and bombarded with 0.35 MeV He^+ ions at varying fluences. The Ultraviolet–Visible-Near-Infrared (UV–Vis-NIR) optical analyses of the polymers following the ion bombardment revealed that He^+ irradiation considerably raises the Urbach energy and decreases the optical bandgap, indicating a rise in electronic defects and structural disorder. On the other hand, the Fourier Transform Infrared (FTIR), Atomic Force Microscopy (AFM), and X-ray Diffraction (XRD) analyses revealed higher levels of structural degradation in the pristine ABPBI samples, suggesting changes brought about by irradiation-induced oxidation and chain scission processes. In contrast, the 1.0 wt% DWCNT-ABPBI composite demonstrated improved optical and structural integrity, retention, and resistance to He^+ ion-induced damage. According to the results, 1.0 wt% DWCNT reinforcement reduces radiation-induced deterioration and offers more protection from energetic ion exposure in the LEO settings. Thus, this work highlights the distinct impact of He^+ ion interactions with ABPBI and the effectiveness of DWCNT inclusion in improving polymer resilience, and it contributes to the fundamental understanding of the polymer composite for radiation shielding applications.

Keywords: Poly(2,5-benzimidazole) (ABPBI) polymer; Structural properties; Optical properties; Low Earth Orbit; Radiation-shielding polymers; Polymer degradation

1. Introduction

Between approximately 160 km and 2000 km above the Earth's surface, the Low-Earth Orbit (LEO) environment is a dynamic and complex region, home to many space-based vehicles, including satellites, space stations, and spacecraft (Gutiérrez et al., 2023; Lu et al., 2019). In this region, spacecraft contend with a harsh radiation environment that can degrade materials used in LEO applications by altering their structural, optical, and functional characteristics. Historically, high-density polyethene (HDPE) and metals like aluminium (Al) have been extensively used for radiation shielding in the space environment. Some limitations of Al and HDPE include a significant increase in

* Corresponding author at: Centre for Space Research, North-West University, Potchefstroom 2531, North West, South Africa.
E-mail address: b.oryema@muni.ac.ug (B. Oryema).

https://doi.org/10.1016/j.asr.2025.08.065
0273-1177/

flight payload and the generation of secondary radiation upon particle impact (Fourie et al., 2023; More et al., 2021; Zeng et al., 2023). Suitable alternatives being explored include polymers and polymer-based composites. Due to their exceptional radiation resistance, high thermal stability, and lightweight nature, poly 2,5-benzimidazole (ABPBI) polymers represent a promising candidate for this study (Fourie et al., 2023; Square et al., 2023).

Notwithstanding these benefits, ABPBI's optical vulnerability is one of its most significant drawbacks. The benzene ring structure of ABPBI inherently absorbs visible light, making the material prone to optical degradation when deployed in the space environment (Banerjee et al., 2023). Additionally, exposure to vacuum ultraviolet (VUV) radiation and energetic charged particles in the LEO environment can alter the ABPBI's efficacy as a shielding material by causing photo-oxidation, polymer chain scission, and changes in optical transmittance (Banerjee et al., 2023; Ghosh & Das, 2023). These degradative effects impact the performance and longevity of ABPBI-based materials in radiation shielding applications. The charged particles in the LEO region originate from various sources, including trapped particles in Van Allen's inner belt, solar wind particles (though rare, due to the strong geomagnetic field shielding effect), and galactic sources in the form of galactic cosmic rays (Fourie et al., 2023; Gutiérrez et al., 2023; Restier-Verlet et al., 2021).

The total population of trapped particles in the inner belt comprises protons (~90 %), electrons (~9 %), and helium ions (He^{+} and He^{2+}), making up about 1 % (Kovtyukh, 2020). Meanwhile, the galactic cosmic ray particles in the LEO environment consist of energetic protons (~87 %), helium ions (~12 %), and electrons and heavy ions (~1%) (Alcaraz et al., 2000; Fourie et al., 2023; Kim et al., 2021; Kovtyukh, 2020; Spjeldvik et al., 1999). Additional sources of charged particles in the LEO are ionospheric plasmas, consisting primarily of electrons and positively charged ions, including singly charged oxygen (O^{+}) and helium (He^{+}) ions, as well as the doubly charged oxygen (O^{++}) ions (Keika et al., 2022). While protons are the most abundant particles in the LEO, helium ions are highly relevant due to their more substantial energy transfer and remarkable ability to induce atomic displacement reactions and material defects (Leblanc et al., 1995).

The current study focuses on 0.35 MeV He^{+} ion irradiation because it represents low-energy He ions trapped in the LEO inner radiation belt, which typically range from eV to ~ 8 MeV (Alcaraz et al., 2000; Kim et al., 2021; Kovtyukh, 2020). Unlike higher-energy He ions, the 0.35 MeV energy ensures examination of defect formation within the polymer bulk rather than full penetration, making it highly relevant for surface and near-surface degradation effects. Stopping and Range of Ions in Matter (SRIM) simulations confirm that at 0.35 MeV, He^{+} ions penetrate ~1–2 μm into the polymer. Previous studies investigated nanofiller reinforcements, primarily employing carbon nanotubes (CNT) to improve the radiation tolerance of ABPBI polymers. For instance, Fourie et al. (Fourie et al., 2023) investigated multi-wall carbon nanotube (MWCNT)-enhanced ABPBI polymers under proton irradiation, demonstrating that MWCNT improves polymer resistance to proton-induced structural degradation and a reduction in secondary neutron generation. This study focuses on double-wall carbon nanotube (DWCNT) reinforcement, helium ion (He^{+}) irradiation, the resulting optical bandgap shifts, Urbach energy variations, structural changes, and polymer chain stability.

2. Materials and methods

2.1. Polymer synthesis

To synthesise the ABPBI polymer, the following reagents were used: AB monomers 3,4-aminobenzoic acid (DABA, 97 %), phosphorus pentoxide (P_2O_5, 99 %), sodium hydroxide (NaOH), methanesulfonic acid (MSA, 99 %), double-walled carbon nanotube (DWCNT), and ethyl alcohol (CH_3CH_2OH, 99.98 %). Fig. 1 shows the step-by-step illustrations of the synthesis process, in which 1.5 g of P_2O_5 and 10 ml of MSA were measured and added into a 150 ml resin flask. The mixtures were thoroughly stirred using a magnetic stirrer at 150°C for one hour under a dry nitrogen purge until a homogeneous solution was obtained. This was followed by adding 1 g of DABA to the reaction mixture to prevent the solution from foaming. The new combination was mixed adequately for 30 min. The new solution was divided into two portions, with the first portion meant to form the pristine ABPBI and the second turned into the DWCNT-ABPBI nanocomposite by adding 1.0 wt% DWCNT load concentration and stirring for an extra hour to obtain a homogenous solution as the reaction temperature was gradually increased from 150 to 200°C.

The pristine and 1.0 wt% DWCNT-enhanced solutions were separately poured into specially built glass moulds with dimensions of 50 mm × 10 mm × 1 mm on a flat hotplate. The moulds were heated to 200°C for 3 h inside a ventilated fume hood to evaporate MSA from the membranes. The membranes were extracted from the moulds by immersing the heated glass moulds in deionised water for 24 hrs. The extracted membranes were removed from the water and put into a purification solution of 50 ml of 0.1 M NaOH, 25 ml of CH_3CH_2OH, and 75 ml of deionised water to remove remnant phosphoric acid from the membranes. The purification process was run for three days, with the solution containing the membranes being continuously stirred while the purification solution changed every 24 h. The membranes were then soaked for 4 h in deionised water to eliminate any residual purification mixture. Lastly, the membranes were removed from the water and placed between two sheets of filter paper to stay flat and ready for irradiation.

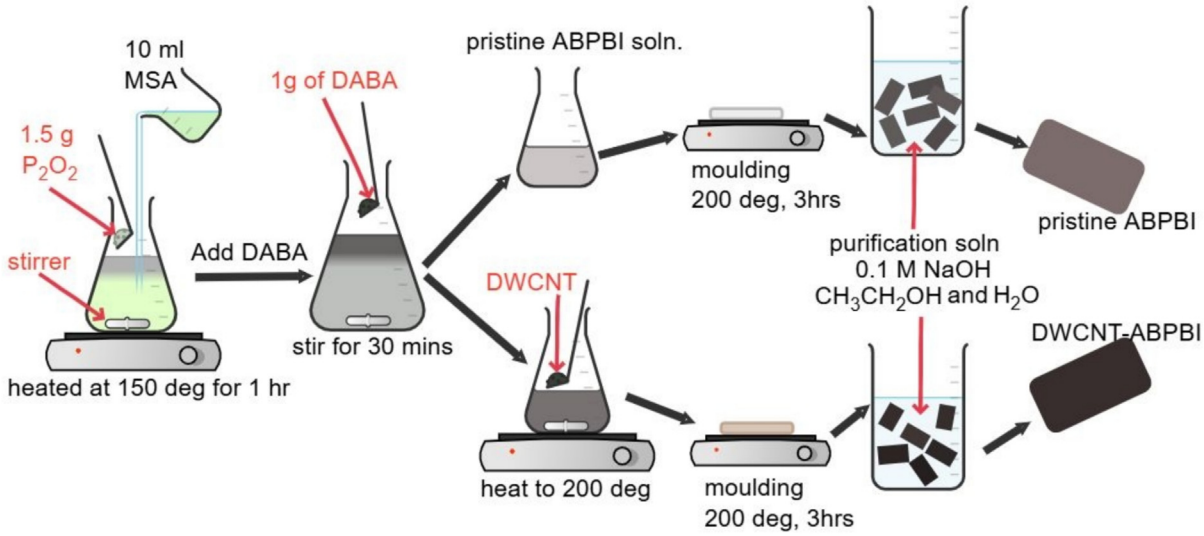

Fig. 1. Synthesis of pristine and DWCNT-ABPBI from DABA in a reaction mixture of MSA and P_2O_5.

2.2. Irradiation

The pristine and the 1.0 wt% DWCNT-ABPBI polymers of uniform thickness of ~300 μm were cut into 1 × 1 cm^2 pieces and exposed to 0.35 MeV He^+ at various fluences of 1 × 10^{12}, 1 × 10^{13}, 1 × 10^{14}, and 1 × 10^{15} ions/cm^2. The irradiation experiment was conducted at room temperature with a constant beam current of 5 nA using the 3 MV Tanden accelerator at iThemba LABS, Cape Town, South Africa.

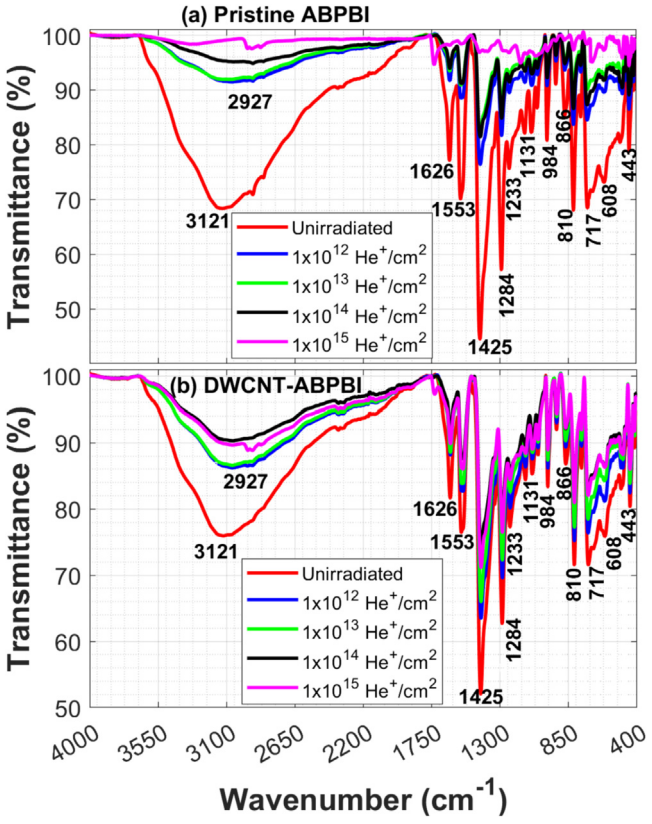

Fig. 2. FTIR spectra of (a) pristine ABPBI and (b) 1.0 wt% DWCNT-ABPBI polymers.

2.3. Characterisation techniques

Radiation-induced changes in the polymers' chemical bond structures following the 0.35 MeV He^+ ion bombardment were carried out using the Fourier Transform Infrared (FTIR) spectrometer type Vertex 80, scanned in the wavenumber range from 4000 to 400 cm^{-1}. The optical measurements were performed at room temperature and ambient pressure using an Ultraviolet–Visible-Near-Infra red (UV–Vis-NIR) Cary 60 spectrophotometer operated in the 200–1000 nm wavelength range and a scan rate of 600 nm per minute. Also, nanoscale evolutions in the surface morphological properties, such as surface topography and surface roughness, were analysed using a Bruker Atomic Force Microscopy (AFM) device operated in the tapping mode at room temperature and ambient atmosphere. Lastly, X-ray diffraction (XRD) analyses of the samples' crystalline structures were performed using a PW3050/60 XRD diffractometer with Co-Kα_1 radiation (λ = 1.17902 Å) operated in the 2-theta degree range of 5–90°. The results are presented and discussed in the following section.

3. Results and discussion

3.1. FTIR spectral analyses

Fig. 2 shows the FTIR spectra for the irradiated and unirradiated pristine and 1.0 wt% DWCNT-ABPBI polymers. In the wavenumber region between 3640 and 1750 cm^{-1}, a broad and major band was observed around 3121 cm^{-1}, and two small bands around 2927 cm^{-1} and between 2380 and 2290 cm^{-1}. The band at 3121 cm^{-1} is

found in all the irradiated and unirradiated pristine and 1.0 wt% DWCNT-ABPBI polymers, except for the pristine polymers exposed to higher fluences of 1×10^{14} He^+/cm^2 and 1×10^{15} He^+/cm^2, where the bands disappeared. This band corresponds to the hydrogen-bonded stretching N–H group and C–H stretching bands in benzene rings (Fourie et al., 2023; Mahjabin et al., 2022). The band at 2927 cm^{-1} is most pronounced in the pristine and 1.0 wt % DWCNT-ABPBI polymers exposed to the highest fluence of 1×10^{15} He^+/cm^2. Furthermore, the small band between 2380–2290 cm^{-1} is only observed in the 1.0 wt% DWCNT-ABPBI (both unirradiated and irradiated) and the unirradiated pristine ABPBI polymers. This peak is assigned to the double-bonded C═N and C═C stretching lattice vibrations.

In the wavenumber region between 1750 and 1300 cm^{-1}, up to three strong bands are observed at 1626, 1553, and 1425 cm^{-1}. These bands are present in all the polymer samples except the pristine polymer irradiated at 1×10^{15} He^+/cm^2, where the peaks are nearly flattened. A small peak emerged around 1740 cm^{-1} in the pristine and 1.0 wt% DWCNT-ABPBI polymers exposed to 1×10^{15} He^+/cm^2. The band at 1626 cm^{-1} is assigned to the C═N/C═C stretching vibrations, and the strong band at 1553 cm^{-1} is assigned to the single-bonded C—C/C—N bending vibrations, resulting from in-plane deformation of the benzimidazole ring (Liu, 2010). The sharpest band at 1425 cm^{-1} is assigned to the stretching and bending vibrations of the single-bonded C—C and C—N structures. Additionally, in the wavenumber region between 1300 and 400 cm^{-1}, which represents the molecular fingerprint region, several bands are observed, with the major ones being at 1284, 1233, 1131, 984, 866, 810, 717, 608, and 443 cm^{-1}. Some of these bands are due to benzene rings, and others are assigned to the single-bonded C—C and C—N stretching and bending vibrational modes and are observed in all the polymers; however, the intensities decreased with increasing He^+ ion fluence, and most of them disappeared in the pristine ABPBI polymer exposed to 1×10^{15} He^+/cm^2.

Generally, the FTIR results show that the absorption band peaks of both polymer categories decreased with increasing He^+ fluence, with the decrease being more drastic and pronounced in the pristine than in the 1.0 wt% DWCNT-ABPBI polymers. This observation suggests that the 1.0 wt% DWCNT-ABPBI polymers are more radiation tolerant than the pristine polymers, and seems to agree with a previous study by Fourie et al. (Fourie et al., 2023), which investigated the effects of proton irradiation on multi-walled carbon nanotube (MWCNT)-enhanced ABPBI polymers. It also agrees with the findings of a study by Square et al. (Square et al., 2023) on the effects of atomic oxygen (AO) irradiation on the properties of pristine and MWCNT-enhanced ABPBI polymer composites. In both previous studies above, the MWCNT-enhanced ABPBI polymers exhibited better structural integrity with increasing ion fluences than the pristine ABPBI polymers. Square et al. (Square et al., 2023) argued that this could be due to the MWCNT acting as barriers, protecting the underlying ABPBI matrices from incident irradiation-induced damage. The reduction in peak intensity with increasing He^+ ion fluences observed in the current study is attributed to irradiation-induced destruction of the imidazole and benzene structures of the polymers due to chain scission (breakage) of the chemical bonds in the polymer matrices, especially for the pristine ABPBI polymers (Abdelhamied et al., 2021; Fourie et al., 2023; Ghosh & Das, 2023; Makuuchi & Cheng, 2011).

3.2. Optical analyses

3.2.1. Optical transmission and absorption spectra

The measured optical transmittance and calculated absorption spectra for the two polymer types are shown in Fig. 3. The absorption spectra data were obtained from transmittance data using the Beer-Lambert relation (Edwards & Alexander, 2016; Mayerhöfer et al., 2020);

$$A = 2 - \log_{10} T(\%), \tag{1}$$

where A is the absorbance, and T is the transmittance in percentage. Fig. 3 reveals a high absorption band, with no transmission in all samples in the 200–550 nm low-wavelength UV–Visible region. The high absorption can be attributed to the UV and visible light carrying sufficient energy to excite valence electrons to transition between orbitals, triggering a series of chemical reactions such as free radical photo-polymerisation (Ribas-Massonis et al., 2022). For organic compounds such as aldehydes (—CHO), ketones (—CO—), alkenes, alkynes, nitriles, aromatic rings, and carbonyl compounds containing σ, π, and n-electrons, light absorption in the UV–Visible region is strictly associated with the $n \rightarrow \pi^*$ and $\pi \rightarrow \pi^*$ electronic transitions in those molecules that contain photon-absorbing functional groups (chromophores) such as C═O, N═O, and C═C groups, and the aromatic rings with valence electrons of low excitation energies (Edwards & Alexander, 2016; Ribas-Massonis et al., 2022).

While electronic transitions involving σ-bonds are allowed, they only occur in the low wavelength region below 200 nm (see Fig. 4). Such transitions require higher energies to drive electrons across the large energy gaps between the bonding and antibonding orbitals. Hence, they are not often captured in UV–Vis spectrometry measurements. Thus, the high absorption spectra observed in this study in the wavelength region of 200–550 nm are attributed to only the $\pi \rightarrow \pi^*$ electronic transitions. Here, unsaturated doubly-bonded π-electrons in the C═C bonds, conjugated C═C—C═C groups, and the unsaturated aromatic benzene rings of the ABPBI structures absorb light and jump from the highest bonding energy levels of the π-orbitals to the lowest energy levels of the empty antibonding π^*-orbitals (Abul-Hail, 2017; Chen et al., 2024) as schematically illustrated in Fig. 4. Since each electron jump takes energy from the photon, the photon energy is

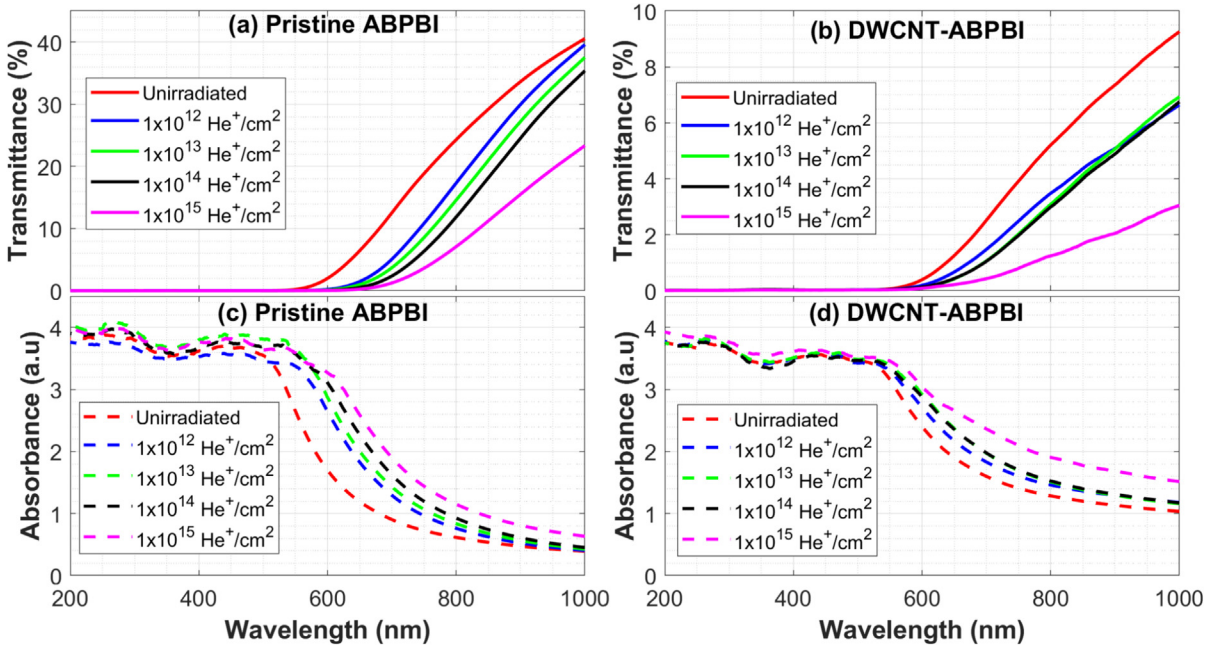

Fig. 3. Optical transmission and absorption spectra of the pristine and 1.0 wt% DWCNT-ABPBI polymers.

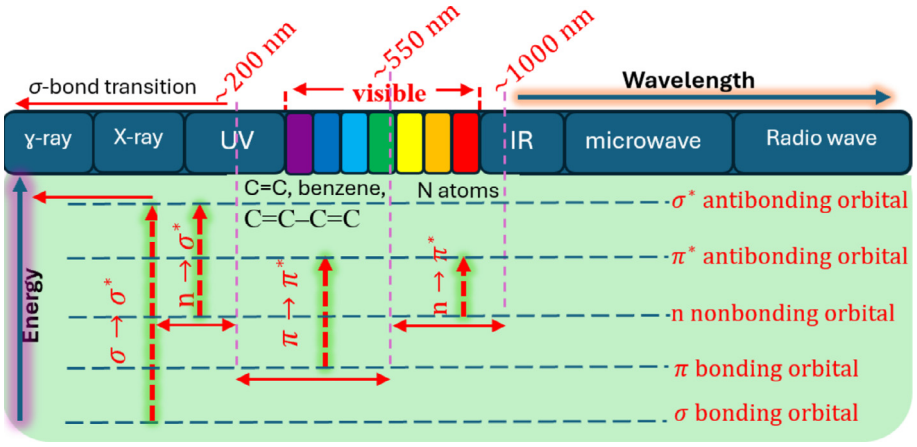

Fig. 4. Schematic illustration of molecular electronic transitions in organic compounds (Ribas-Massonis et al., 2022).

completely absorbed and used to promote the electrons. This also explains the zero transmission observed in this study in this wavelength region.

Fig. 3 also shows that photon transmission increased (i.e., absorption decreased) exponentially in the Vis-NIR wavelength region of 550–1000 nm in all the samples, with the increase being more drastic in the pristine than in the 1.0 wt% DWCNT-ABPBI polymers. This is directly attributed to the presence of DWCNTs, which are strong absorbers that introduce extrinsic absorption edges to the material's band structures. Also, the weak absorption (i.e., enhanced transmission) in this region is linked to the narrow energy band n → π^* transitions, in which lone pair electrons jump from the non-bonding n-orbital to the antibonding π^*-orbitals (Abul-Hail, 2017; Chen et al., 2024) as illustrated in Fig. 4. These transitions are associated with the nitrogen atoms in the polymer compositions (Edwards & Alexander, 2016). The observed differences in optical spectra (absorption and transmission) of the samples with increasing He^+ ion fluences are ascribed to radiation-induced formation of new defects or electronic levels in the forbidden band regions of the polymer materials. These defects are linked to bond-breakage due to scission and the subsequent formation of free radicals, carbonaceous clusters, and extended systems of conjugated unsaturated structures, which could have modified the band structures of the polymer materials (Abul-Hail, 2017; Lal & Quamara, 2014; Singh & Samra, 2008).

3.2.2. Absorption coefficient, penetration depth, and photon energy

Other parameters that are vital in describing the nature of electron transitions and the variations in band structures of the polymers following the He^+ ion bombardment, such

as the absorption coefficient (α) and penetration depth (δ) were analysed in this study. The values of α were obtained from the optical transmission data using the relation (Abul-Hail, 2017);

$$\alpha = -\frac{1}{d}\ln\left(\frac{T}{100}\right), \tag{2}$$

where T is the transmittance, and d is the thickness of the polymers, which is $\approx 300\mu m$. The parameter, α provides information about the passage of light through matter by measuring the decrease in the light intensity per unit depth of the material (Al-Attiyah et al., 2019). The values of δ are derived from α using the relation (Mahjabin et al., 2022);

$$\delta = \frac{1}{\alpha} \tag{3}$$

The parameter, δ defines the thickness of a material at which the incident photon intensity falls to 37 % of the initial intensity at the surface. It helps characterise photon absorption within a material. Lastly, the photon energy ($h\nu$), which is an important parameter for calculating the optical bandgaps, was obtained from the relation (Alyamani & Mustapha, 2016; Oryema et al., 2022);

$$h\nu = \left(\frac{hc}{\lambda}\right) = \left(\frac{1243}{\lambda}\right)\text{eV}, \tag{4}$$

where λ and ν are the photon wavelength and frequency, respectively, and h is Planck's constant. A relation showing the dependence of α and δ on $h\nu$ is shown in Fig. 5.

As seen from Fig. 5, the absorption coefficient, α, for all samples increased sharply with increasing photon energy through the range of 1.2 eV to 2.4 eV. This represents the high absorption edge, and it is credited to the enhancement of charge carriers in the materials (Al-Attiyah et al., 2019). As the incident photon energy increases, more valence electrons with energy close to the bandgap absorb and utilise this energy to transition from the bonding (π) or non-bonding n-orbitals to the free antibonding π^*-orbitals in the conduction bands (Issa et al., 2021; Mahjabin et al., 2022). This is evident by the drastic decrease in the values of penetration depth, δ, with increasing photon energy. In the photon energy range of 2.4–6.2 eV, the absorption coefficient and penetration depth curves are nearly flattened, indicating that the absorption coefficient saturates in higher energy regions where the incident photon energy is completely absorbed and utilised to drive electronic transitions between orbitals. Lastly, the observed dependence of α and δ on the He^+ ion fluences, with a redshift towards lower energy in the range of 1.2 eV and 2.4 eV, is attributed to radiation-induced enhancements in the quantity of charge carriers within the polymer materials (Abdelhamied et al., 2021; Abul-Hail, 2017).

3.2.3. Optical bandgap analyses

The optical bandgap (E_g), also known as the forbidden bandwidth, is the energy difference between the bottom of the conduction band (CB) and the top of the valence band (VB) of a material (Chen et al., 2024). This parameter is vital for analysing the processes of excitation, movement, and the subsequent transition of photogenerated electrons in materials (Chen et al., 2024; Mahjabin et al., 2022). In the current work, the effects of He^+ ion bombardment on the optical bandgaps of the polymers were analysed according to Tauc's relation (Basha & Basha, 2017; Oryema et al., 2022; Tommalieh et al., 2022);

$$(\alpha h\nu)^{1/n} = B(h\nu - E_g), \tag{5}$$

where B is a constant between 10^5 and 10^6 cm^{-1} eV^{-1}, often called the band tailing parameter (Issa et al., 2021), $h\nu$ is the photon energy, E_g is the energy bandgap, and n is the transition coefficient whose value signifies the character of the electronic transition. For direct transition, n assumes

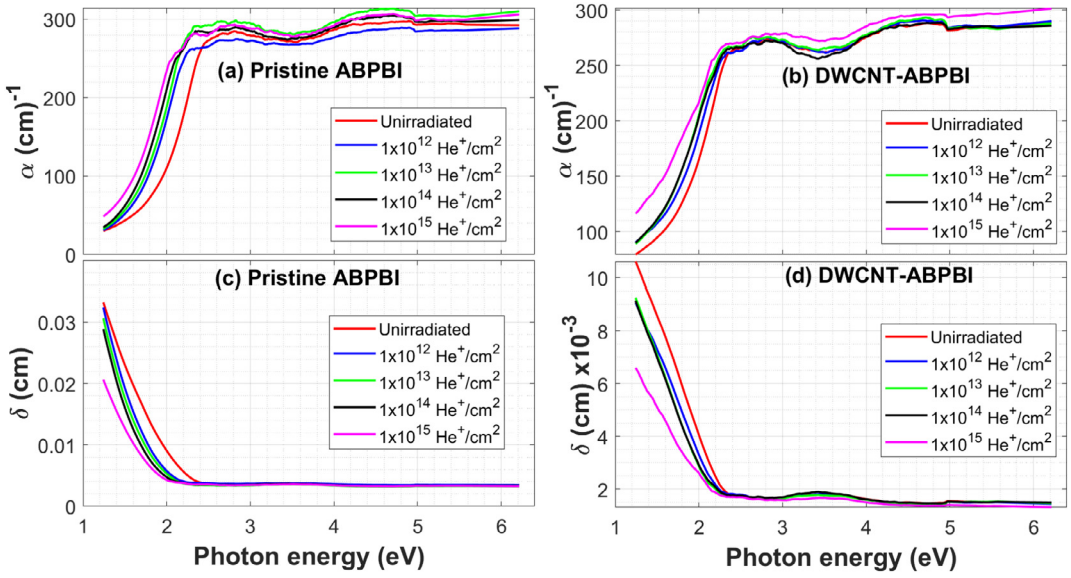

Fig. 5. Absorption coefficients and penetration depths of pristine and 1.0 wt% DWCNT-ABPBI polymers.

definite values of 1/2 or 3/2, while for indirect transition, n is 2 or 3, depending on whether the transition is allowed or forbidden for each pair of values (Singh & Samra, 2008; Tommalieh et al., 2022).

By plotting $(\alpha h\nu)^{1/n}$ against $h\nu$ for the allowed direct and indirect transitions, then extrapolating the straight parts of the plots at higher $h\nu$ to the $h\nu$ axes, the direct ($E_{g,\mathrm{dir}}$) and indirect ($E_{g,\mathrm{ind}}$) optical bandgaps were estimated from the intercept of the fitting line in Fig. 6, and the extracted values are presented in Table 1. Table 1 shows that the values of $E_{g,\mathrm{dir}}$ and $E_{g,\mathrm{ind}}$ for both the pristine and 1.0 wt% DWCNT-ABPBI polymers decrease with increasing ion fluences. This decrease can be attributed to radiation-induced bond rupturing and the subsequent formation of new defect states or unsaturated bonds, which are rich in charge carriers and require less energy to cause the $\pi \rightarrow \pi^*$ and $n \rightarrow \pi^*$ electronic transitions between different molecular orbitals (Abdelhamied et al., 2021; Basha & Basha, 2017). Table 1 also shows that the bandgaps of 1.0 wt% DWCNT-ABPBI polymers have lower values than for pristine polymers, further suggesting that the presence of DWCNT nanofillers in the polymer matrix introduced disordered structures, which created more localised states in the forbidden gaps.

3.2.4. Number of carbon atoms

The number of carbon atoms per carbonaceous cluster (M) was calculated from E_g through the relation (Singh & Samra, 2008);

$$E_g = \frac{34.3}{\sqrt{M}} \tag{6}$$

This is particularly done to quantify radiation-induced clustered disorders. Also, the number of dissociated carbon atoms per conjugation length (N), which provides information about the linear orientation of detached carbon atoms, was estimated using Robertson's relation (Lal & Quamara, 2014);

$$N = \frac{2\beta\pi}{E_g}, \tag{7}$$

where $\pi = 3.14$ and 2β is the energy associated with a pair of adjacent π sites. The value of β is taken to be 2.9 eV as it is associated with $\pi - \pi^*$ optical transitions in –C=C– structures (Singh & Samra, 2008). Table 2 summarises the calculated values of M and N for both the pristine and 1.0 wt% DWCNT-ABPBI polymers. Table 2 shows that both M and N increased with increasing He^+ ion fluence in both polymer categories, suggesting more isolated carbon atoms in the irradiated than in the unirradiated polymers. This further confirms the C–H bond breakages as evident in FTIR results, and the resulting release or escape of hydrogen as hydrogen molecules due to irradiation-induced thermal spikes in the polymer chains (Lal & Quamara, 2014; Singh & Samra, 2008). These carbonaceous clusters and conjugates are rich in charge carriers and are thus responsible for reducing the bandgaps of the irradiated polymers.

3.2.5. Urbach energy analyses

In principle, a semiconductor is only supposed to absorb photons whose energies are above its bandgap energy, E_g, and is to be transparent to photons below this threshold. However, it has been established that the density of states

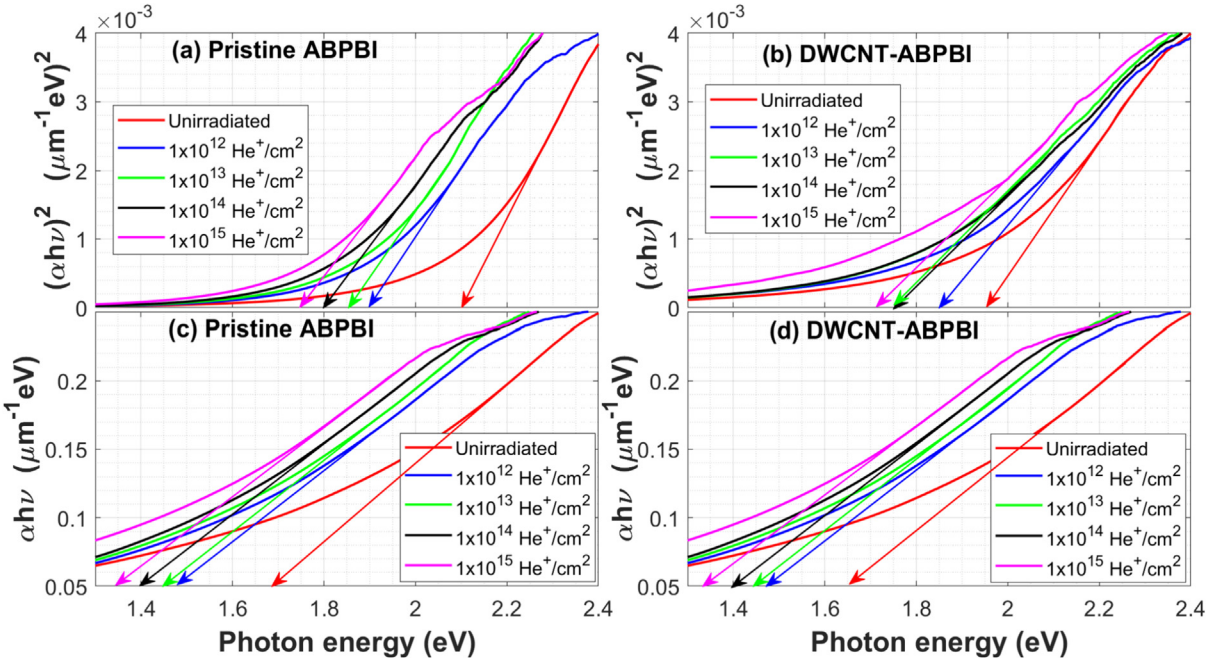

Fig. 6. (a) Direct bandgap of pristine ABPBI, (b) direct bandgap of 1.0 wt% DWCNT-ABPBI, (c) indirect bandgap of pristine ABPBI, and (d) indirect bandgap of 1.0 wt% DWCNT-ABPBI.

Table 1
Direct and indirect bandgaps of the pristine and 1.0 wt% DWCNT-ABPBI polymers.

	Pristine ABPBI		DWCNT-ABPBI	
Ion fluence (He^+/cm^2)	$E_{g,dir}$ (eV)	$E_{g,ind}$ (eV)	$E_{g,dir}$ (eV)	$E_{g,ind}$ (eV)
Unirradiated	2.10	1.70	1.95	1.65
1×10^{12}	1.90	1.47	1.85	1.46
1×10^{13}	1.86	1.45	1.75	1.44
1×10^{14}	1.80	1.40	1.75	1.40
1×10^{15}	1.75	1.35	1.72	1.34

Table 2
The values of E_U, and M and N for the direct and indirect bandgaps.

	Pristine ABPBI					DWCNT-ABPBI				
Ion fluence (He^+/cm^2)	M_{dir}	N_{dir}	M_{ind}	N_{ind}	E_U (eV)	M_{dir}	N_{dir}	M_{ind}	N_{ind}	E_U (eV)
Unirradiated	267	8	407	10	0.53	309	9	432	11	0.72
1×10^{12}	326	9	544	11	0.54	344	10	552	12	0.77
1×10^{13}	340	10	560	12	0.59	384	10	567	13	0.83
1×10^{14}	363	10	600	13	0.64	384	10	600	13	0.94
1×10^{15}	384	11	646	13	0.76	398	11	655	14	0.97

of semiconductors tends to broaden further from the bandgap near the absorption edge, and the energy associated with such tail absorption, the Urbach energy (E_U) is less than the optical bandgap (Abdelhamied et al., 2021; Kaiser et al., 2021). This energy emanates from static disorders resulting from structural imperfections, and dynamic disorders resulting from thermal lattice vibrations and exciton/electron–phonon interactions (Subha et al., 2023). Fig. 7 illustrates the broadening of the density of states of semiconductors near the absorption edge and the corresponding increase in absorbance with increasing energy.

Thus, to further confirm the existence of radiation-induced defect states in the band regions of the two categories of polymer materials, the current study estimated the Urbach energy, E_U by correlating the absorption coefficient, α using the relation (Abdelhamied et al., 2021; Abulyazied et al., 2024; Subha et al., 2023);

$$\ln\alpha = \ln\alpha_o + \left(\frac{1}{E_U}\right)h\nu \tag{8}$$

where α_o is a constant representing the absorption coefficient value in defect-free material, and $h\nu$ is the incident photon energy. The E_U values were estimated by plotting the graphs of $\ln\alpha$ against $h\nu$ below the absorption edges and getting the inverse of the slopes of the obtained straight lines of the plots. Table 2 contains the obtained values of E_U, and it shows that for both polymers, E_U increased with the increasing He^+ ion fluence, while portraying inverse relationships with bandgap values and direct linear relationships with the number of carbon atoms. The increase in E_U values confirms the existence of radiation-induced growth in the number of novel localised states, such as carbon clusters in the forbidden regions, which resulted in exotic band tails close to the band edges of the polymers (Abulyazied et al., 2024). Table 2 also shows that the 1.0 wt% DWCNT-ABPBI polymers recorded higher E_U values than the corresponding pristine polymers, affirming that DWCNT fillers increased the concentration of disordered atoms and defects in the structural bonding.

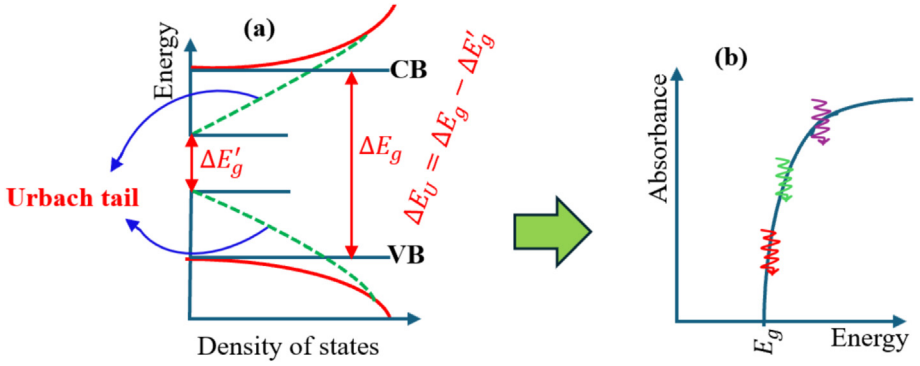

Fig. 7. Schematic illustrations of (a) broadening of the density of states due to Urbach band tails, and (b) increase in absorbance with increasing energy (Khan et al., 2021).

3.3. AFM analyses

Figs. 8 and 9 are 3D AFM micrographs showing radiation-induced alterations in surface topographies of the pristine and 1.0 wt% DWCNT-ABPBI polymers, respectively, recorded over the representative sample surface area of 25 μm × 25 μm. The unirradiated pristine ABPBI polymer in Fig. 8**(a)** has a spiny rough surface characterised by intertwined hummocks and pinhole-like features. When exposed to increasing He^+ ion fluences, the surface topography decreased with the increase in ion fluence, as depicted in Fig. 8**(b)–(e)**. In Fig. 8**(e)**, the hillocks have crumbled, and the polymer surface is nearly flat, with small and compact surface grains. Similar observations can be made of the 1.0 wt% DWCNT-ABPBI polymers in Fig. 9. Quantitative quantification of the evolution in surface properties of the polymers was performed by analysing and comparing the average surface roughness, R_a, which is simply the deviation of a surface from the mean height. As seen from the sub-captions of the 3D micrographs in Figs. 8 and 9, R_a similarly decreased with increasing He^+ ion fluence, implying radiation-induced surface smoothening.

The decrease in R_a is credited to cumulative radiation-induced surface melting and chain scission processes (Singh & Kumar, 2019). During the ion bombardment experiment, the incident particles interact with and transfer a significant portion of their energies to the target atoms, leading to atomic excitation and vibration. This induces localised heating or thermal spikes in the polymer structures, causing the polymer surfaces to melt and the chains in the polymer's amorphous regions to undergo scission (Oryema et al., 2020, 2022). This produces smaller grains that easily relocate to fill the surface loopholes, thus reducing surface topography or roughness. By comparing the R_a values of the pristine and 1.0 wt% DWCNT-ABPBI polymers in Fig. 8 and Fig. 9, respectively, it is observed that

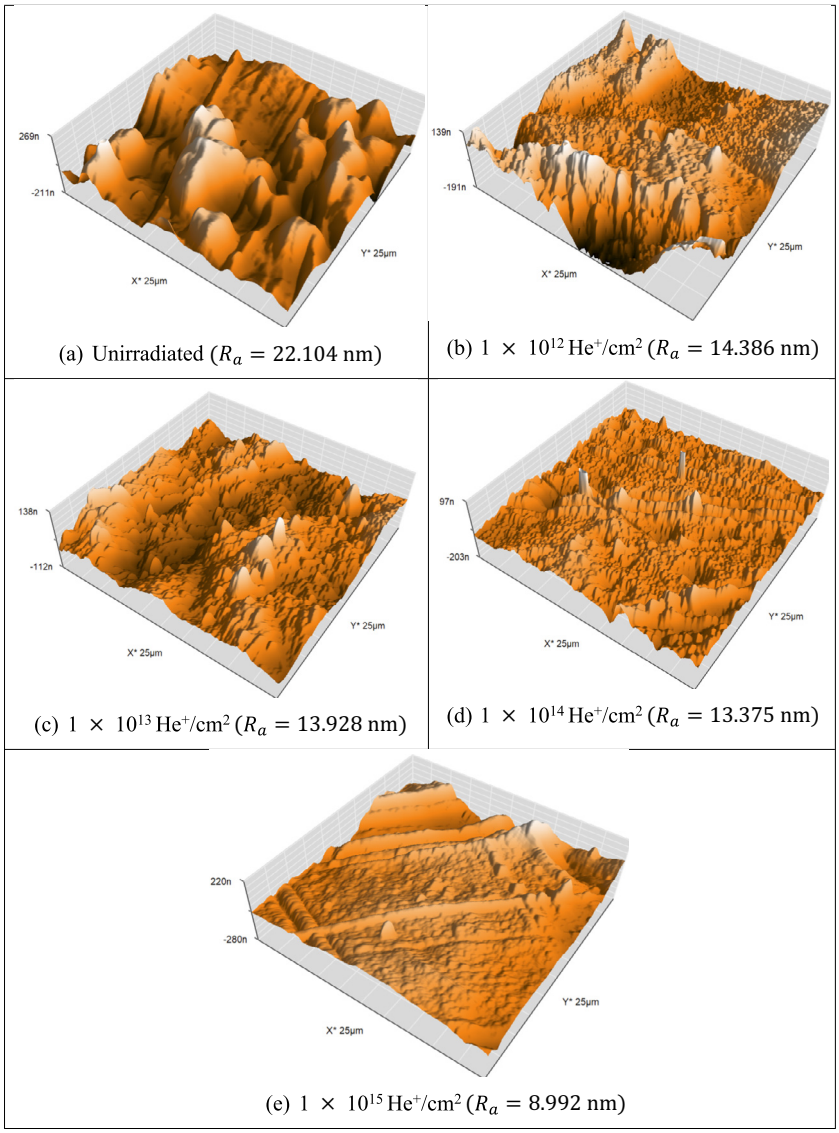

Fig. 8. 3D AFM micrographs of the pristine ABPBI polymers under 0.35 MeV He^+ bombardment.

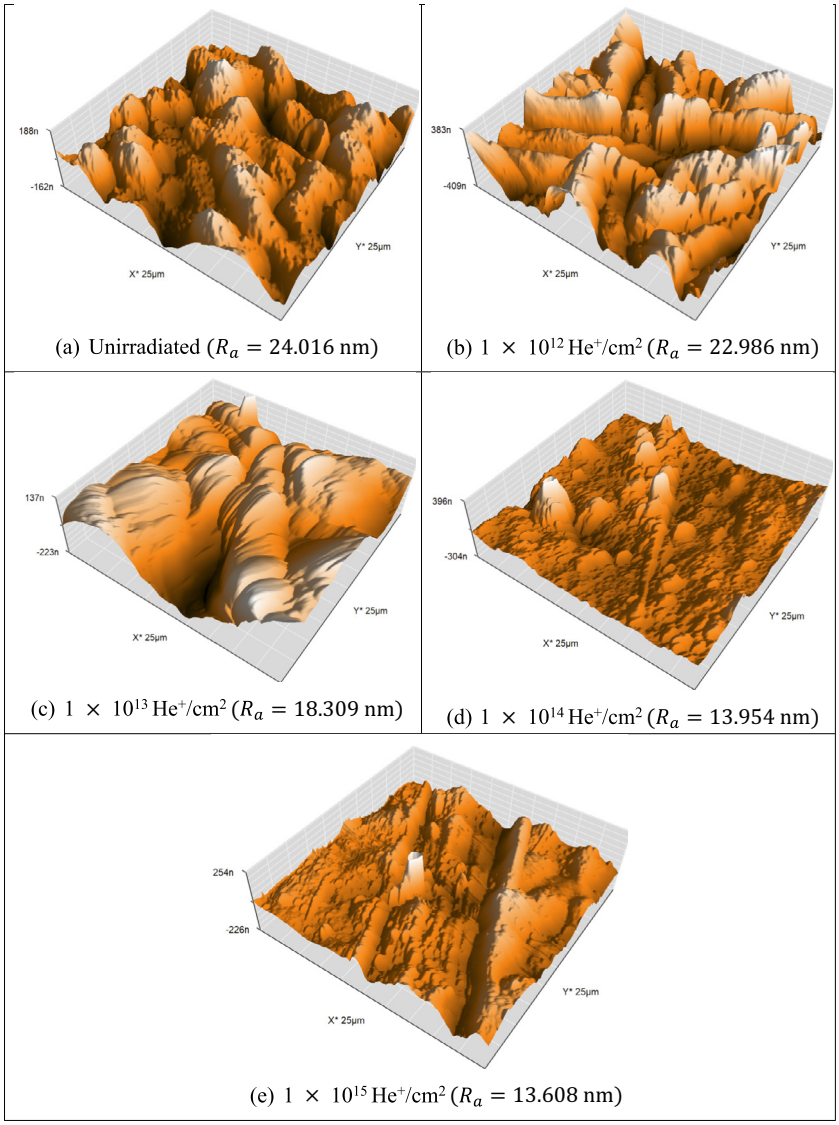

Fig. 9. 3D AFM micrographs of 1.0 wt% DWCNT-ABPBI polymers under 0.35 MeV He^+ ion bombardment.

the He^+ ion affected the pristine polymers more profoundly than the 1.0 wt% DWCNT-ABPBI polymers, as evident by the lower values of R_a in the pristine samples. This observation is attributed to the coercive ability of the DWCNT nanofillers, which act as barriers to protect the underlying polymer matrices from incident irradiation-induced damages (Square et al., 2023), implying 1.0 wt% DWCNT-ABPBI polymers are more tolerant to radiation than the pristine ABPBI polymers.

3.4. XRD analyses

The XRD spectra of the pristine and 1.0 wt% DWCNT-ABPBI polymers are presented in Fig. 10 **(a)** and **(b),** respectively. These spectra reveal the semi-crystalline nature of both polymer categories, with diffraction peaks typical of the ABPBI backbone structures appearing at $2\theta \approx 11.2^{o}$ and a more ordered peak at $2\theta \approx 26.5^{o}$ (Fourie et al., 2023; Liu, 2010). These 2θ values correspond to the diffraction planes (1 1 0) and (3 1 1), respectively. No new peaks are formed, nor are any existing peaks destroyed, in either sample following the He^+ ion bombardment. This implies that the 0.35 MeV He^+ ion bombardment did not destroy the ABPBI backbone structures, nor did it add impurities to both polymers. Fig. 10 also shows the adverse impact of the 0.35 MeV He^+ ion bombardment on the crystalline structures of both polymer types, manifested as radiation-induced amorphisation or a decrease in diffraction peak intensities with increasing ion fluences. The spectral decline is attributed to radiation-induced defects within the polymer materials (Kumar et al., 2012). The interactions between the incident He^+ ion and the polymer atoms may result in atomic excitations and other energy exchange mechanisms that

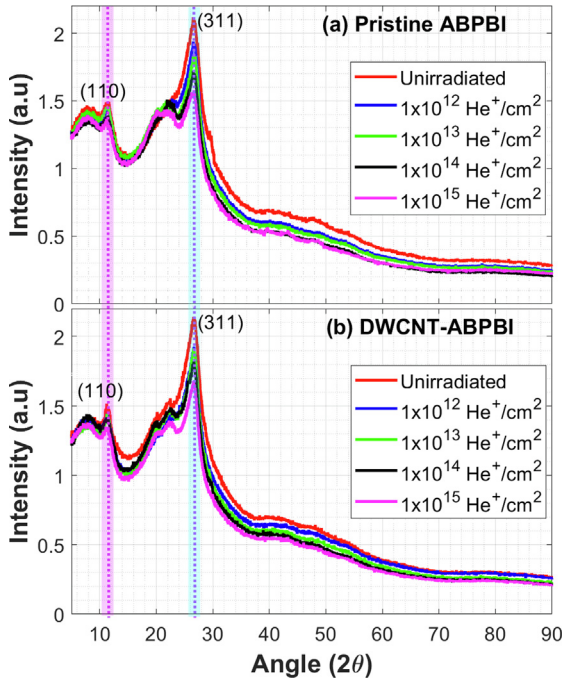

Fig. 10. XRD spectra of (a) the pristine and (b) 1.0 wt% DWCNT-ABPBI polymers bombarded with 0.35 MeV He^+ ions.

generate localized heating within the polymers. This initiates chain scission reactions and the subsequent formation and accumulation of defect states such as vacancies and interstitials, which give rise to disordered lattice orientations, peak broadening, and a reduction in crystallinity.

The crystallite size, D, which is a useful parameter for quantifying the dimensions of the diffracting domains in a crystalline material, was estimated in this study by using the Scherrer relation (Kumar et al., 2012; Oryema et al., 2020, 2022);

$$D = \frac{k\lambda}{\beta\cos\theta}, \tag{9}$$

where, λ is the diffracted X-ray wavelength (λ = 1.17902 Å), θ is the Bragg angle, β is the full width at half maximum (FWHM) of the diffraction peaks in radians, and k is the Scherrer constant ($k = 0.94$). Tables 3 and 4 contain the calculated D values for the pristine and 1.0 wt% DWCNT-ABPBI polymers, respectively. They also contain other vital lattice parameters such as the lattice spacing or d-spacing, and FWHM values for the diffraction planes (1 1 0) and (3 1 1). The 2θ values in Tables 3 and 4 generally follow a similar trend, revealing continuous shifts in peak positions toward larger angles with increasing ion fluence. This is followed by a general decrease in lattice spacings and an increase in crystallite sizes. Such behaviours of crystalline materials under ion bombardment indicate the presence of compressive strain in the crystal planes (Chandramohan et al., 2007; Oryema et al., 2022). This further confirms the accumulation of radiation-induced defects in the polymer materials.

4. Future works

While this study provides valuable insights into the effects of 0.35 MeV He^+ ion bombardment on the pristine

Table 3
XRD parameters of pristine ABPBI polymers.

Fluence (He^+/cm^2)	(110) plane				(311) plane			
	2θ(°)	d-spacing (nm)	β (rad)	D (nm)	2θ(°)	d-spacing (nm)	β (rad)	D (nm)
Unirradiated	11.205	0.7890	0.0183	6.0743	26.384	0.33753	0.0206	5.51924
1×10^{12}	11.231	0.7872	0.0179	6.2298	26.524	0.33578	0.0205	5.55467
1×10^{13}	11.258	0.7853	0.0177	6.2966	26.541	0.33557	0.0202	5.64620
1×10^{14}	11.261	0.7851	0.0174	6.3942	26.544	0.33553	0.0197	5.77774
1×10^{15}	11.415	0.7746	0.0170	6.5524	26.549	0.33547	0.0188	6.05953

Table 4
XRD parameters of 1.0 wt% DWCNT-ABPBI polymers.

Fluence (He^+/cm^2)	(110) plane				(311) plane			
	2θ(°)	d-spacing (nm)	β (rad)	D (nm)	2θ(°)	d-spacing (nm)	β (rad)	D (nm)
Unirradiated	11.126	0.7946	0.0174	6.3935	26.541	0.3356	0.020645	5.5210
1×10^{12}	11.284	0.7835	0.0165	6.7494	26.568	0.3352	0.019249	5.9158
1×10^{13}	11.294	0.7828	0.0155	7.1664	26.568	0.3352	0.019242	5.9180
1×10^{14}	11.310	0.7817	0.0151	7.3949	26.646	0.3343	0.019234	5.9211
1×10^{15}	11.415	0.7746	0.0148	7.5087	26.673	0.3339	0.019176	5.9397

and 1.0 wt% DWCNT-ABPBI polymers, it's important to note that the helium spectra in the space environment span a broad energy range (keV to GeV levels). Thus, to fully assess the composites' durability in LEO, future work should investigate the effects of these energy spectra, as they may induce different defect dynamics in matter. Also, conducting multi-ion exposure studies, analysing the synergistic effects of space environmental stressors and vacuum-level variations, and evaluating the mechanical properties, as well as space-based testing and validation of materials, should be considered in future works. Other future works shall involve the use of advanced analytical techniques such as the Positron Annihilation Lifetime Spectroscopy (PALS) to quantify irradiation-induced nanoscale defects and free volume or structural changes in the material, Scanning Electron Microscope (SEM) for high-resolution surface morphological analyses of material surfaces to reveal ion-induced modifications such as cracking, blistering, or roughening, Transmission Electron Microscope (TEM) to reveal irradiation-induced amorphization, crystallization, or bubble formation, and Focused Ion Beam (FIB) technique to reveal subsurface damages such as buried interfaces and ion implantation zones, and to reconstruct 3-dimensional damage profiles in irradiated materials.

5. Conclusion

The impacts of 0.35 MeV He^+ ion bombardment on the optical and structural properties of pristine and 1.0 wt% DWCNT-ABPBI polymers are examined in this work. The main conclusions are that in pristine ABPBI, He^+ irradiation causes structural disorder, an increase in Urbach energy, and a decrease in the bandgap, all of which indicate progressive material degradation. By reducing defect formation and maintaining optical properties, DWCNT reinforcement significantly enhances polymer resilience.

AFM analyses confirmed a continuous smoothing of surface topography and surface roughness with increasing He^+ fluence, attributed to radiation-induced surface melting and polymer chain scission. Pristine ABPBI surfaces became nearly smooth and flat at high fluences, while DWCNT-ABPBI retained more textured features, indicating better resistance to morphological changes. This resistance is due to the protective, energy-dissipating role of DWCNTs, which act as barriers to radiation-induced surface and bulk damage. The XRD results confirmed the adverse effects of the He^+ ion bombardment on the ordered structures of the polymers, revealing radiation-induced amorphisation as the result of accumulated defects.

The ion beam energy used in this study correlates with the trapped He^+ ion energy levels frequently found in the radiation belts and LEO conditions. Recent studies have attempted to increase ABPBI's radiation tolerance by adding nanofillers. In this investigation, DWCNT-ABPBI polymers demonstrated improved structural integrity and reduced optical degradation compared to their pristine counterparts, which implies that some of the adverse effects are lessened by DWCNT reinforcement.

Declaration of competing interests

The authors declare the following financial interests/personal relationships which may be considered as potential competing interests: Lynndle Square reports financial support was provided by the South African National Research Foundation (NRF). If there are other authors, they declare that they have no known competing financial interests or personal relationships that could have appeared to influence the work reported in this paper.

Acknowledgments

The authors acknowledge the NRF-iThemba LABS, Cape Town, South Africa, for providing the beamtime for the ion bombardment experiment. We also acknowledge the financial support from NRF through the Thuthuka Fund [UID No. 138417].

References

Abdelhamied, M.M., Atta, A., Abdelreheem, A.M., Farag, A.T.M., El Sherbiny, M.A., 2021. Oxygen ion induced variations in the structural and Linear/Nonlinear optical properties of the PVA/PANI/Ag nanocomposite film. Inorg. Chem. Commun. 133 (September). https://doi.org/10.1016/j.inoche.2021.108926 108926.

Abul-Hail, R.C., 2017. Optical limiting behavior correlated with the surface and etching time of irradiated nuclear track detector. J. Mater. Sci. Mater. Electron. 28 (3), 2311–2316. https://doi.org/10.1007/s10854-016-5798-1.

Abulyazied, D.E., Issa, S.A.M., Saudi, H.A., Abomostafa, H.M., Zakaly, H.M.H., 2024. Dysprosium-enriched polymer nanocomposites: Assessing radiation shielding and optical properties. Opt. Mater. 153 (May). https://doi.org/10.1016/j.optmat.2024.115604 115604.

Al-Attiyah, K.H.H., Hashim, A., Obaid, S.F., 2019. Fabrication of novel (carboxy methyl cellulose–polyvinylpyrrolidone–polyvinyl alcohol)/lead oxide nanoparticles: structural and optical properties for gamma rays shielding applications. Int. J. Plast. Technol. 23 (1), 39–45. https://doi.org/10.1007/s12588-019-09228-5.

Alcaraz, J., Alpat, B., Ambrosi, G., Anderhub, H., Ao, L., Arefiev, A., Azzarello, P., Babucci, E., Baldini, L., Basile, M., et al., 2000. Helium in near-Earth orbit. Phys. Lett. Section B 494, 193–202.

Alyamani, A., Mustapha, N., 2016. Effects of high-dose gamma irradiation on ITO thin film properties. Thin Solid Films 611, 27–32. https://doi.org/10.1016/j.tsf.2016.05.022.

Banerjee, P.S., Chanda, J., Ghosh, P., Mukhopadhyay, R., Das, A., Banerjee, S.S., 2023. Electron beam radiation technology application in the tyre industry. In: Chowdhury, S.R. (Ed.), Applications of High Energy Radiations: Synthesis and Processing of Polymeric Materials. Springer Nature, Singapore, pp. 41–77. https://doi.org/10.1007/978-981-19-9048-9_2.

Basha, A.F., Basha, M.A., 2017. Impact of neutron irradiation on the structural and optical properties of PVP / gelatin blends doped with dysprosium (III) chloride. J. Appl. Phys. 235104 (122).

Chandramohan, S., Sathyamoorthy, R., Sudhagar, P., Kanjilal, D., Kabiraj, D., Asokan, K., 2007. Swift heavy ion beam irradiation

induced modifications in structural, morphological, and optical properties of CdS thin films. Nucl. Inst. Methods Phys. Res. B 254, 236–242. https://doi.org/10.1016/j.nimb.2006.11.041.

Chen, L., Gao, Z., Li, Q., Yan, C., Zhang, H., Li, Y., Liu, C., 2024. A review: Comprehensive investigation on bandgap engineering under high pressure utilizing microscopic UV-Vis absorption spectroscopy. APL Mater. 12 (3). https://doi.org/10.1063/5.0196152.

Edwards, A.A., Alexander, B.D., 2016. UV-visible absorption spectroscopy, organic applications. In: Encyclopedia of Spectroscopy and Spectrometry, 3rd ed. Elsevier Ltd.. https://doi.org/10.1016/B978-0-12-803224-4.00013-3.

Fourie, L.F., Square, L., Arendse, C., Msimanga, M., 2023. ABPBI/MWCNT for proton radiation shielding in low earth orbit. APL Mater. 11 (7). https://doi.org/10.1063/5.0156686.

Ghosh, S.K., Das, N.C., 2023. Application of radiation curing on properties and performance of polymers and polymer composites. In: Chowdhury, S.R. (Ed.), Applications of High Energy Radiations: Synthesis and Processing of Polymeric Materials. Springer Nature, Singapore, pp. 1–39. https://doi.org/10.1007/978-981-19-9048-9_1.

Gutiérrez, O., Prieto, M., Perales-Eceiza, A., Ravanbakhsh, A., Basile, M., Guzmán, D., 2023. Toward the use of electronic commercial off-the-shelf devices in space: assessment of the true radiation environment in low earth orbit (LEO). Electronics (Switzerland) 12 (19). https://doi.org/10.3390/electronics12194058.

Issa, S.A., Zakaly, H.M.H., Pyshkina, M., Mostafa, M.Y.A., Rashad, M., Soliman, T.S., 2021. Structure, optical, and radiation shielding properties of PVA–BaTiO3 nanocomposite films: an experimental investigation. Radiat. Phys. Chem. 180. https://doi.org/10.1016/j.radphyschem.2020.109281 109281.

Kaiser, C., Sandberg, O.J., Zarrabi, N., Li, W., Meredith, P., Armin, A., 2021. A universal Urbach rule for disordered organic semiconductors. Nat. Commun. 12 (1), 1–9. https://doi.org/10.1038/s41467-021-24202-9.

Keika, K., Kasahara, S., Yokota, S., Hoshino, M., Seki, K., Amano, T., Kistler, L.M., Nosé, M., Miyoshi, Y., Hori, T., Shinohara, I., 2022. Preferential energization of lower-charge-state heavier ions in the near-earth magnetotail. J. Geophys. Res. Space Phys. 127 (1). https://doi.org/10.1029/2021JA029786.

Khan, M., Alam, M.S., Saha, B., Ahmed, S.F., 2021. Synthesis and characterization of cadmium sulfide (CdS) thin films by cyclic voltammetry technique. Mater. Today Proc. 47 (July), 2351–2357. https://doi.org/10.1016/j.matpr.2021.04.316.

Kim, K.H., Kwon, H.J., Lee, J., Jin, H., Seough, J., 2021. A case study of transversely heated low-energy helium ions by EMIC waves in the plasmasphere. J. Geophys. Res. Space Phys. 126 (2), 1–16. https://doi.org/10.1029/2020JA028560.

Kovtyukh, A.S., 2020. Earth's radiation belts' ions: patterns of the spatial-energy structure and its solar-cyclic variations. Ann. Geophys. 38 (1), 137–147. https://doi.org/10.5194/angeo-38-137-2020.

Kumar, V., Sonkawade, R.G., Chakarvarti, S.K., Singh, P., Dhaliwal, A. S., 2012. Carbon ion beam induced modifications of optical, structural and chemical properties in PADC and PET polymers. Radiat. Phys. Chem. 81 (6), 652–658 10.1016/j.radphyschem.2012.02.027.

Lal, S., Quamara, J.K., 2014. Effects of 100 MeV O7+ ion beam irradiation on the optical, chemical and structural properties of NCO-terminated polybutadiene based liquid crystalline polyurethane. Vacuum 105, 7–10. https://doi.org/10.1016/j.vacuum.2014.01.028.

Leblanc, L., Ross, G.G., Wallace, W.E., 1995. Measured stopping powers of hydrogen and helium in polystyrene near their maximum values. Nuclear Inst. Methods Phys. Res., B 95 (4), 457–462. https://doi.org/10.1016/0168-583X(94)00606-7.

Liu, Q. 2010. Poly(2, 5-benzimidazole)-based polymer electrolyte membranes for high-temperature fuel cell applications. https://repository.lboro.ac.uk/articles/thesis/Poly_2_5-benzimidazole_-based_polymer_electrolyte_membranes_for_high-temperature_fuel_cell_applications/9230696.

Lu, Y., Shao, Q., Yue, H., Yang, F., 2019. A review of the space environment effects on spacecraft in different orbits. IEEE Access 7, 93473–93488. https://doi.org/10.1109/ACCESS.2019.2927811.

Mahjabin, S., Haque, M., Sobayel, K., Selvanathan, V., Jamal, M.S., Bashar, M.S., Sultana, M., Hossain, M.I., 2022. Investigation of morphological, optical, and dielectric properties of RF sputtered WOx thin films for optoelectronic applications. Nanomater. Art. 12, 3467.

Makuuchi, K., Cheng, S., 2011. Radiation Processing of Polymer Materials and its Industrial applications. Radiation Processing of Polymer Materials and Its Industrial Applications. https://doi.org/10.1002/9781118162798.

Mayerhöfer, T.G., Pahlow, S., Popp, J., 2020. The bouguer-beer-lambert law: shining light on the obscure. ChemPhysChem 21, 2029–2046. https://doi.org/10.1002/cphc.202000464.

More, C.V., Alsayed, Z., Badawi, M.S., Thabet, A.A., Pawar, P.P., 2021. Polymeric composite materials for radiation shielding: a review. Environmental Chemistry Letters, Vol. 19. Springer International Publishing. https://doi.org/10.1007/s10311-021-01189-9.

Oryema, B., Jurua, E., Madiba, I.G., Ahmad, I., Aisida, S.O., Ezema, F. I., Maaza, M., 2022. Effects of 7 MeV proton irradiation on microstructural, morphological, optical, and electrical properties of fluorine-doped tin oxide thin films. Surfaces and Interfaces, Vol. 28. Springer. https://doi.org/10.1016/j.surfin.2021.101693.

Oryema, B., Jurua, E., Madiba, I.G., Nkosi, M., Sackey, J., Maaza, M., 2020. Effects of low-dose γ-irradiation on the structural, morphological, and optical properties of fluorine-doped tin oxide thin films. Radiat. Phys. Chem. 176. https://doi.org/10.1016/j.radphyschem.2020.109077.

Restier-Verlet, J., El-Nachef, L., Ferlazzo, M.L., Al-Choboq, J., Granzotto, A., Bouchet, A., Foray, N., 2021. Radiation on Earth or in space: what does it change? Int. J. Mol. Sci. 22 (7). https://doi.org/10.3390/ijms22073739.

Ribas-Massonis, A., Cicujano, M., Duran, J., Besalú, E., Poater, A., 2022. Free-Radical Photopolymerization for Curing Products for Refinish Coatings Market. Polymers 14 (14), 1–21. https://doi.org/10.3390/polym14142856.

Singh, L., Samra, K.S., 2008. Opto-structural characterization of proton (3 MeV) irradiated polycarbonate and polystyrene. Radiat. Phys. Chem. 77, 252–258. https://doi.org/10.1016/j.radphyschem.2007.05.009.

Singh, P., Kumar, R., 2019. Radiation Physics and Chemistry of Polymeric Materials. In: Kumar, V., Chaudhary, B., Sharma, V., Verma, K. (Eds.), Radiation Effects in Polymeric Materials. Springer International Publishing, pp. 35–68. https://doi.org/10.1007/978-3-030-05770-1_2.

Spjeldvik, W.N., Fritz, T.A., Sheldon, R.B., Chen, J., 1999. Magnetic local time survey of radiation belt helium ion structure conducted with data from the polar cammice / hit instrument. Phys. Chem. Earth, Part C: Solar, Terrest. Planet. Sci. 24 (1–3), 233–238. https://doi.org/10.1016/S1464-1917(98)00034-8.

Square, L., Fourie, L.F., Ellis, E., Msimanga, M., 2023. Effects of atomic oxygen irradiation on the structural and thermal properties of ABPBI/MWCNT composites. In: Proceedings of the IEEE Conference on Nanotechnology. https://doi.org/10.1109/NANO58406.2023.10231300.

Subha, T.D., Prabu, R.T., Parasuraman, S., Kumar, A., 2023. Role of Urbach energy in controlling the voltage output of solar cells. Opt. Quant. Electron. 55 (9), 1–11. https://doi.org/10.1007/s11082-023-05067-2.

Tommalieh, M.J., Barakat, M.M.E., Bahareth, R.A., Mahrous, E.M., Aldawood, S., Nouh, S.A., 2022. Thermal, optical, and color modification in makrofol VLG 7-1 nuclear track detector due to gamma irradiation. J. Macromol. Sci. Part B Phys. 61 (3), 491–505. https://doi.org/10.1080/00222348.2022.2052456.

Zeng, C., Kang, Q., Duan, Z., Qin, B., Feng, X., Lu, H., Lin, Y., 2023. Development of Polymer Composites in Radiation Shielding Applications: A Review. In: Mano, R. (Ed.), Journal of Inorganic and Organometallic Polymers and Materials, Vol. 33. Springer US. https://doi.org/10.1007/s10904-023-02725-6, Issue 8.